Chapter 9
Weak Focusing Synchrotron

Abstract This Chapter is a brief introduction to the weak focusing synchrotron, and to the theoretical material needed for the simulation exercises. It relies on basic charged particle optics and acceleration concepts introduced in the previous Chapters, and further addresses
- fixed closed orbit,
- periodic structures,
- periodic stability,
- optical functions,
- synchrotron motion,
- depolarizing resonances.

The simulation of weak synchrotrons only require a very limited number of optical elements; actually two are enough: DIPOLE or BEND to simulate combined function dipoles, and DRIFT. Particle monitoring requires keywords introduced in the previous Chapters, including FAISCEAU, FAISTORE, possibly PICKUPS. Spin motion computation and monitoring resort to SPNTRK, SPNPRT, FAISTORE,

Notations used in the Text

B; $\mathbf{B}$; B_x, B_y, B_s	field value; field vector; components
$B\rho = p/q$; $B\rho_0$	particle rigidity; reference rigidity
C	closed orbit length, $C = 2\pi R$
E	particle energy
EFB	Effective Field Boundary
f_{rf}	RF frequency
h	RF harmonic number
m; m_0; M	mass; rest mass; in units of MeV/c^2
$n = \frac{\rho}{B}\frac{dB}{d\rho}$	focusing index, a local quantity
$\mathbf{p}$; p_0	particle momentum vector; reference momentum
P_i, P_f	initial, final asymptotic polarization at traversal of a spin resonance
q	particle charge
r	orbital radius
R	average radius, $R = C/2\pi$
s	path variable
v	particle velocity
V(t); $\hat{V}$	oscillating voltage; its peak value
x, x', y, y'	radial and axial coordinates in Serret-Frénet frame
$\beta = v/c$; β_0; β_s	normalized particle velocity; reference; synchronous
$\gamma = E/m_0$	Lorentz relativistic factor
Δp, δp	momentum offset
ε_u	Courant-Snyder invariant (u: x, r, y, l, Y, Z, s, etc.)
ϵ_R	strength of a depolarizing resonance
ϕ; ϕ_s	particle phase at voltage gap; synchronous phase
ϕ_z	betatron phase advance, z stands for x or y
φ	spin angle to the vertical axis
$\langle A\rangle$; $\langle A\rangle\|_u$	average of A; over variable u

Introduction

The synchrotron is an outcome the phase focusing concept [1, 2], combined with constant orbit acceleration [3]. Phase focusing states that off-crest acceleration with proper phase of the voltage oscillation at arrival of a particle at the accelerating gap results in stable longitudinal motion, “longitudinal focusing”, around a stable, fixed, “synchronous phase”. The reference orbit in a synchrotron on the other hand, is maintained at constant radius by ramping the guide field in synchronism with the acceleration, a concept already familiar at the time with the betatron [4].

Phase focusing was demonstrated experimentally in 1946 using a cyclotron dipole [5]. Demonstration of phase stability at constant orbital radius followed in

1946, using an existing betatron ring [6]. Due to the cycling of the acceleration, a synchrotron accelerates particle bunches, comprised of particles that have proper relationship, in both frequency and phase, with the oscillating voltage at the accelerating gap, or gaps around the ring. The concept allowed greatest energy reach, it led to the construction of a series of proton rings with increasing energy: 1 GeV at Birmingham (1953), 3.3 GeV at the Cosmotron (BNL, 1953), 6.2 GeV at the Bevatron (1954), 10 GeV at the Synchro-Phasotron (Dubna, 1957), and a few additional ones beyond 1952~1953, into the era of the technology which would essentially dethrone it: the strong focusing synchrotron. The general layout of these first synchrotrons included straight sections (often 4, Fig. 9.1), which allowed insertion of injection (Fig. 9.2) and extraction systems, accelerating cavities, orbit correction and beam monitoring equipment.

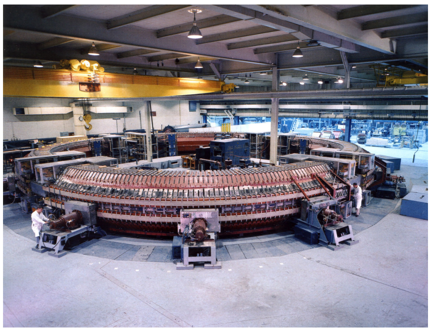

Fig. 9.1 The Cosmotron at BNL, reached its full design energy of 3.3 GeV in 1953. It was used until 1968 [8]

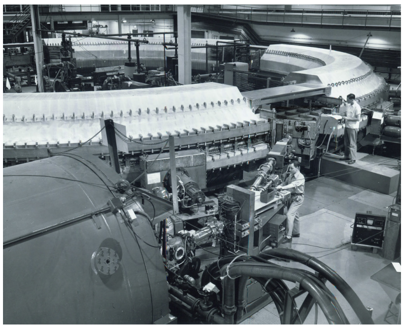

Fig. 9.2 Details of the low energy injection line and injection straight section at the Cosmotron [9]

9.1 Basic Concepts and Formulæ

The synchrotron is based on two key principles: a varying magnetic field to maintain the accelerated bunch on a constant orbit, with constant transverse focusing, namely,

$$\mathrm{B(t)} = \mathrm{p(t)/q}, \quad \rho = \text{constant} \tag{9.1}$$

and longitudinal phase stability, possibly including modulation of the accelerating voltage frequency in order to follow the velocity change of the bunch [1, 2]. The modulation of the oscillating voltage frequency is maintained in synchronism with the bunch revolution motion, of which the period varies with time following

$$f_{RF}(t) = hf_{rev}(t) \tag{9.2}$$

with h an integer, the "RF harmonic". Since the orbit is maintained unchanged turn after turn, the revolution frequency varies, in inverse proportion to particle velocity. These are two major evolutions compared to the cyclotron, where, instead, the magnetic field and the oscillating voltage frequency are fixed.

The synchronism between RF voltage frequency and revolution time (Eq. 9.2) allows maintaining the bunch at an appropriate phase, the "synchronous phase", with respect to the oscillating voltage when passing the accelerating gap (this is discussed in a next Section).

Synchronous acceleration is technologically simpler in the case of electrons, as frequency modulation is unnecessary beyond a few MeV of particle energy. For instance, from $v/c = 0.9987$ at 10 MeV to $v/c \to 1$ at very high energy, the relative change in revolution frequency amounts to $\delta f_{\mathrm{rev}}/f_{\mathrm{rev}} = \delta\beta/\beta < 0.0013$.

Constant closed orbit reduces the radial extent of individual guiding magnets compared to a cyclotron dipole which must encompass a spiraling orbit, and leads to a circular string of dipoles, a ring structure. An archetype of a weak focusing synchrotron ring is shown in Fig. 9.3, Saturne I, a 3 GeV, 4-period, 68.9 m circumference, transverse index focusing synchrotron at Saclay [10]. Operation at Saturne I started in 1957, plans for the acceleration of polarized beams at the time motivated theoretical investigation of resonant depolarization [11]. The four dipoles of the squared ring are 1150 tons each; the straight sections are 4 m long; injection is in the north one (foreground), from a 3.6 MeV Van de Graaff (not visible); the south section houses the extraction system; a beam detection system is located in the east straight; the RF cavity is in the west one and provides a peak voltage of a few kW, whereas the peak power requested from the RF system for acceleration does not exceed 2 kW.

For the sake of comparison: a synchro-cyclotron dipole is a pair of full, massive cylindrical poles; greater energy requires greater radial extent of the magnet to allow the necessary increase of the bend field integral (namely, $\oint B\,dl = 2\pi R_{max}\hat{B} = p_{max}/q$ - note that $\hat{B}$ can be pushed to ~ 2 T as the field is fixed) and accordingly of the diameter of the bulky cylinder, thus the volume of iron increases more than quadratically with bunch rigidity.

A second example of a weak focusing synchrotron is shown in Figure 9.4, the ZGS at Argonne, a 12 GeV, 4-period, 172 m circumference, zero-gradient synchrotron: ZGS had the particularity of using wedge focusing to ensure transverse beam stability. ZGS was operated over 1964-1979, polarized beam acceleration happened in July 1973, to 8.5 GeV/c, and up to 12 GeV/c in the following years [12]. Pulsed quadrupoles were used to pass through several depolarizing intrinsic resonances, a method known as resonance crossing by fast "tune-jump". ZGS proton injector was comprised of a 20 keV source, followed by a 750 keV Cockcroft-Walton and a 50 MeV linac.

The acceleration is cycled in a synchrotron, from injection to top energy, repeatedly. The cycling of the magnetic field, in synchronism with the acceleration voltage, maintains a constant orbit; the field law $B(t)$ depends on the type of power supply. If the ramping uses a constant electromotive force, then

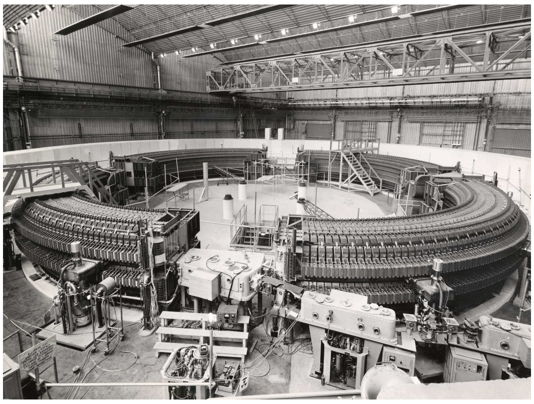

Fig. 9.3 Saturne I at Saclay [10], a 3 GeV, 4-period, 68.9 m circumference, weak focusing synchrotron, field index $n \approx 0.6$ [13]

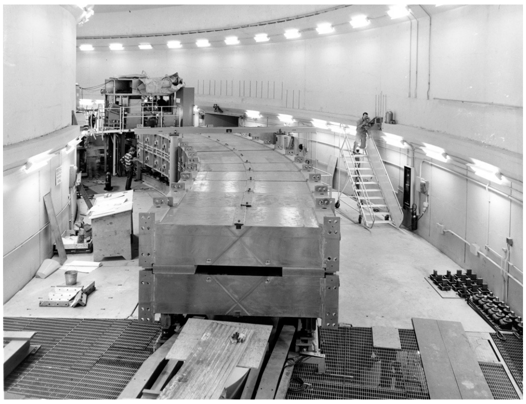

Fig. 9.4 The ZGS at Argonne during construction. A 12 GeV, 4-period, 172 m circumference, wedge focusing synchrotron. Two persons can be seen standing on the left and on the right of the ring, in the background, giving an idea of the size of the magnets

$$B(t) \propto (1 - e^{-\frac{t}{\tau}}) = 1 - \left[1 - \left(\frac{t}{\tau}\right) + \left(\frac{t}{\tau}\right)^2 - \ldots\right] \approx \frac{t}{\tau} \tag{9.3}$$

essentially linear. In that case $\dot{B} = dB/dt$ does not exceed a few Tesla/second, thus the repetition rate of the acceleration cycle if of the order of a Hertz.

If the magnet winding is part of a resonant circuit the field law has the form

$$B(t) = B_0 + \frac{\hat{B}}{2}(1 - \cos \omega t) \tag{9.4}$$

so that, in the interval of half a voltage repetition period, namely $t : 0 \longrightarrow \pi/\omega$, the field increases from an injection threshold value to a maximum value at highest rigidity, $B(t) : B_0 \longrightarrow B_0 + \hat{B}$. The latter determines the highest achievable energy: $\hat{E} = pc/\beta = q\hat{B}\rho c/\beta$. The repetition rate with resonant magnet cycling can reach a few tens of Hertz.

In both cases anyway B imposes its law and the other quantities comprising the acceleration cycle (RF frequency in particular) will follow B(t).

For the sake of comparison again: in a synchrocyclotron the field is constant, acceleration can be cycled as fast as the voltage system allows; assume a conservative 10 kVolts per turn, thus of the order of 10,000 turns to 100 MeV, with velocity $0.046 < v/c < 0.43$ from 1 to 100 MeV, proton. Take $v \approx 0.5c$ to make it simple, an orbit circumference below 30 meter, thus the acceleration takes of the order of $10^4 \times C/0.5c \approx$ms range, potentially a repetition rate in kHz range, more than an order of magnitude beyond what a rapid-cycling pulsed synchrotron allows.

The next decades following the invention of the synchrotron saw an all-out breakthrough, with applications in many fields of science, in medicine, industry. The weak focusing synchrotron allowed colliding particle beams of highest energies on fixed targets in nucleus fission and particle production experiments, leading to the discovery of several fundamental particles. Its technological simplicity still makes it an appropriate technology today in low energy beam application when relatively low beam current is not a concern: it essentially requires a single type of a simple dipole magnet, an accelerating gap, some command-control instrumentation, and that's it! whereas it procures greater beam manipulation flexibilities compared to (synchro-)cyclotrons.

Transverse beam stability in a weak focusing synchrotron ring inherits from the cyclotron techniques, focusing in the dipoles results from the presence of a transverse field gradient $0 < n < 1$ and/or from wedge focusing, as in the aforementioned two examples, Saturne 1 synchrotron [14] and the ZGS [7].

A weak focusing synchrotron is comprised of a string of dipoles separated by field free drift spaces, forming a $\frac{2\pi}{N}$-symmetric, N-periodic structure. Each period ensures a $\frac{2\pi}{N}$ fraction of the 2π bending. N=4 for instance in Saturne I (Fig. 9.3) and in ZGS (Fig. 9.4). In the ZGS a period is comprised of a pair of 45 degree dipoles, a total of 8 dipoles around the ring, whereas Saturne I features a single 90 degree dipole per period, 4 dipoles in total.

Introducing straight sections in the magnetic structure of the ring allows room for inserting the various devices that garnish a synchrotron and contribute beam manipulation flexibility: an accelerating cavity, injection and extraction systems, beam diagnostics equipment, special optical elements, tune jump quadrupoles possibly for polarized beam handling, etc.

9.1.1 Transverse Stability

The introduction to transverse stability in this Section leans on the weak focusing concepts introduced in the Classical Cyclotron Chapter (Chap. 4). Radial motion stability around a reference closed orbit in an axially symmetric dipole field requires the geometrical configuration of particle orbits sketched in Fig. 9.6, resulting from magnetic rigidity $B \times \rho$ an increasing function of radius, which, on the closed orbit (radius = ρ_0), expresses as $\frac{\partial B\rho}{\partial \rho} \geq 0$, viz. $1 + \frac{\rho}{B_0}\frac{\partial B}{\partial \rho} \geq 0$. Vertical stability requires the gap height to increase with radius, thus field decreases with radius, $\frac{\partial B_y}{\partial \rho} < 0$

(Fig. 4.9). This is the focusing method which was used in the classical cyclotron (Sec. 4.2.2). Introduce the field index

$$n = -\frac{\rho_0}{B_0} \frac{\partial B_y}{\partial \rho}\bigg|_{x=0,\ y=0} \tag{9.5}$$

This results in the typical magnet segment shown in Fig. 9.5.

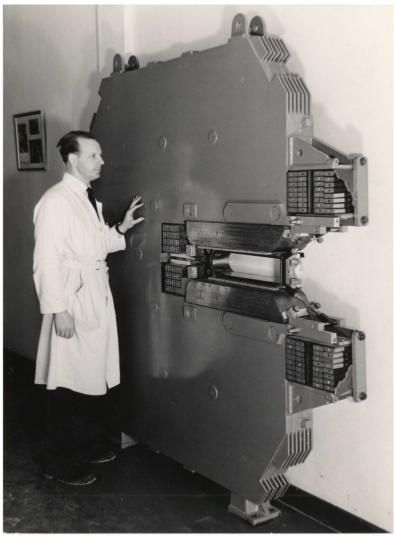

Fig. 9.5 A segment of Saturne I weak focusing synchrotron magnet, with its hardly visible gap tapering (greater outward) to satisfy the weak index condition $0 < n < 1$ [13]

Transverse motion stability in an axially symmetric structure, with or without drift spaces, thus summarizes in

$$0 < n < 1 \tag{9.6}$$

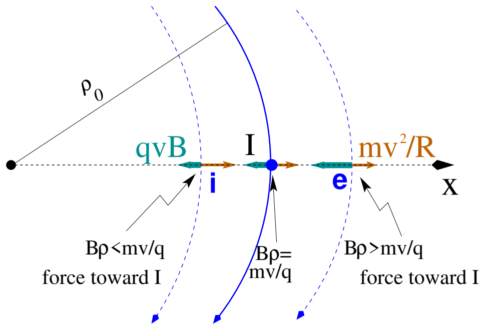

Fig. 9.6 Radial motion stability in an axially symmetric structure. The resultant $F_t = -qvB + mv^2/r$, is zero at I: $B_0\rho_0 = mv/q$. The resultant at i is toward I if $qvB_i < mv^2/\rho_i$, *i.e.* $B_i\rho_i < mv/q$; the resultant at e is toward I if $qvB_e > mv^2/\rho_e$, *i.e.* $B_e\rho_e > mv/q$

Adding drift spaces requires defining two radii, namely,

(i) the magnet curvature radius ρ_0 (Fig. 9.7),

(ii) an average radius $\mathrm{R} = C/2\pi = \rho_0 + \mathrm{Nl}/\pi$ (with C the length of the reference closed orbit and $2l$ the drift length) (Fig. 9.8) which also writes

$$R = \rho_0(1 + k), \qquad k = \frac{Nl}{\pi\rho_0} \tag{9.7}$$

The reference orbit is comprised of arcs of radius ρ_0 in the magnets, and straight segments along the drift spaces that connect these arcs. Adding drift spaces decreases the average focusing around the ring. Trajectories of different momenta are parallel.

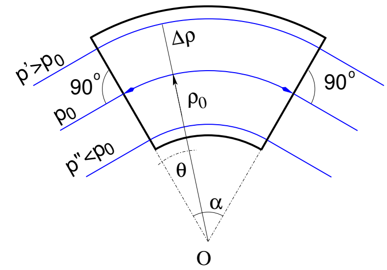

Fig. 9.7 In a sector dipole with radial index $n \neq 0$, closed orbits follow arcs of constant B. A closed orbit at $p_0 + \Delta p$ follows an arc of radius $\rho_0 + \Delta\rho$, $\Delta\rho = \Delta p/(1+n)qB_0$

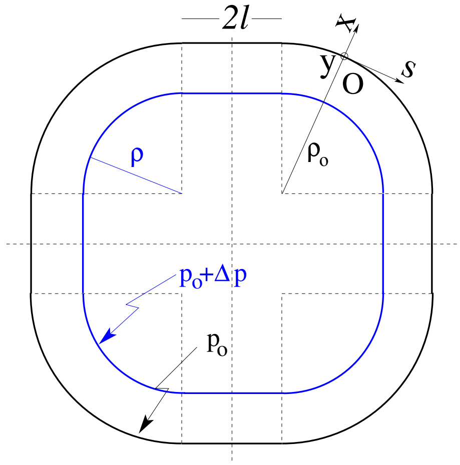

Fig. 9.8 A $2\pi/4$ axially symmetric structure with four drift spaces. Orbit length on reference momentum p_0 is $C = 2\pi\rho_0 + 8l$. (O;s,x,y) is the moving frame, along the reference orbit. The orbit for momentum $p = p_0 + \Delta p$ ($\Delta p < 0$, here) is at constant distance $\Delta \mathrm{x} = \frac{\rho_0}{1-\mathrm{n}}\frac{\Delta \mathrm{p}}{\mathrm{p}_0} = \frac{\mathrm{R}}{(1+\mathrm{k})(1-\mathrm{n})}\frac{\Delta \mathrm{p}}{\mathrm{p}_0}$ from the reference orbit

Geometrical focusing:

In a constant field dipole (radial field index n=0), the longer (respectively shorter) path in the magnetic field for parallel trajectories entering the magnet at greater (respectively smaller) radius results in geometrical focusing. Referring to Fig. 9.9, this effect can be cancelled, *i.e.*, the deviation made the same whatever the entrance radius, if the curvature center is made independent of the entrance radius: OO′ = 0, O′′O = 0. This requires trajectories at an outer (inner) radius to experience a smaller (greater) field so to satisfy $BL = B\rho\alpha = C^{st}$. Differentiating $\mathrm{B}\rho = \mathrm{C}^{\mathrm{st}}$ yields $\frac{\Delta \mathrm{B}}{\mathrm{B}} + \frac{\Delta\rho}{\rho} = 0$, with $\Delta\rho = \Delta x$. Thus the field B(x) must satisfy $\mathrm{n} = -\frac{\rho_0}{\mathrm{B}_0}\frac{\Delta \mathrm{B}}{\Delta \mathrm{x}} = 1$ in order to cancel the geometrical focusing resulting from the curvature.

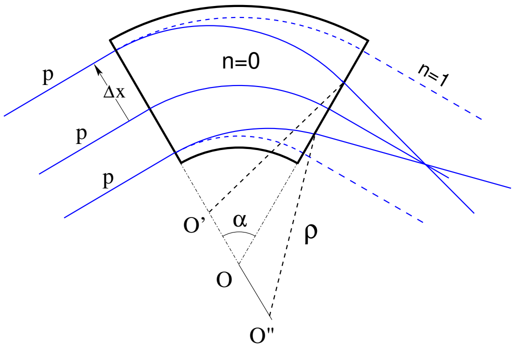

Fig. 9.9 Geometrical focusing: in a sector dipole with focusing index n = 0, parallel incoming rays of equal momenta experience the same curvature radius ρ, they exit converging, as a results of the longer path of outer trajectories in the field, compared to inner ones. An index value n=1 cancels that effect: rays exit parallel

Focal distance associated with the curvature:

Assume n=0, reference radius $\rho = \rho_0$, reference arc length $\mathcal{L} = \rho_0\alpha$. From $\frac{d^2x}{ds^2} + \frac{1}{\rho_0^2}x = 0$ one gets

$$\Delta x' = \int \frac{d^2x}{ds^2}ds \approx -\frac{x}{\rho_0^2}\int ds = -\frac{x}{\rho_0^2}\mathcal{L} \quad \stackrel{def.}{\equiv} -\frac{x}{f} \quad \Rightarrow f = \frac{\rho_0^2}{\mathcal{L}} \tag{9.8}$$

Optical drawbacks of the weak focusing method are, the weakness of the focusing and the absence of independent radial and axial focusing.

Wedge Focusing

This is the focusing method in the ZGS. Profiling the magnet gap in order to adjust the focal distance complicates the magnet; n=0, a parallel gap, makes it simpler. In the ZGS the focal distance is designed based on proper entrance and exit wedge angles (Fig. 9.10): opening the magnetic sector increases the horizontal focusing (and decreases the vertical focusing); closing the magnetic sector has the reverse effect.

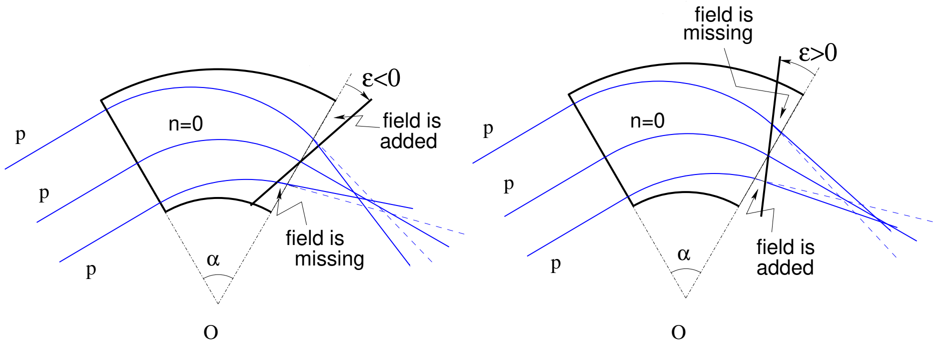

Fig. 9.10 Left: a focusing wedge ($\varepsilon < 0$ by convention); opening the sector increases the horizontal focusing. Right: a defocusing wedge ($\varepsilon > 0$ by convention); closing the sector decreases the horizontal focusing. The focal distance of the bend plane respectively decreases, increases. The effect is the opposite in the vertical plane, opening/closing the sector decreases/increases the vertical focusing.

Vertical focusing at the EFB

The magnetic field falls off smoothly in the fringe field region at the ends of a magnet, from its value in the body to zero at some distance from the iron. The extent of the fall-off is commensurate with the gap size, its shape depends on such factors as the profiling of the iron at the EFB (Fig. 9.11) or the positioning and shape of the coils.

From an optics standpoint, the main effect of the fringe field is the existence of a longitudinal component of the field, $\mathbf{B}_s(s)$. In a mid-plane symmetry dipole, $\mathbf{B}_s(s)$ is non-zero off the median plane, and normal to the iron (Fig. 9.11).

The focal distance f associated with a wedge angle ϵ (Fig. 9.10) satisfies

$$\frac{1}{f} = \tan\frac{\epsilon}{\rho_0} \tag{9.9}$$

with $\epsilon > 0$ if the sector is closing, by convention. In a point transform approximation, at the wedge the trajectory undergoes a local deviation proportional to the distance to the optical axis, namely,

$$\Delta x' = \frac{\tan\epsilon}{\rho_0}\Delta x, \quad \Delta y' = -\frac{\tan\epsilon}{\rho_0}\Delta y \tag{9.10}$$

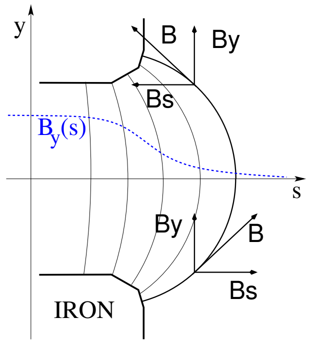

Fig. 9.11 Field components in the $B_y(s)$ fringe field region at a dipole EFB

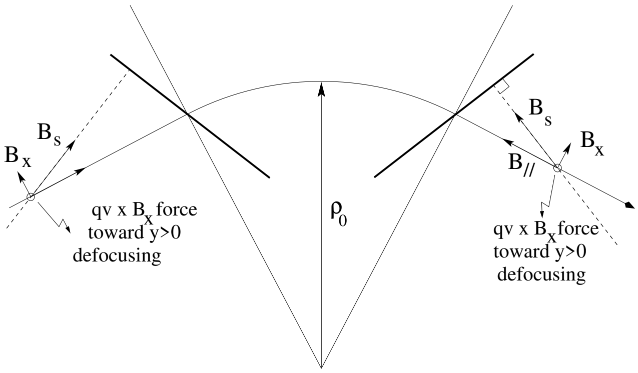

Fig. 9.12 Field components in the fringe field region at the end of a dipole ($y > 0$, here, referring to Fig. 9.11). $B_{//}$ is parallel to the particle velocity. This configuration is vertically defocusing: a charged particle traveling off mid-plane is pulled away from the the latter under the effect of $\mathbf{v} \times \mathbf{B}_x$ force component. Inspection of the $y < 0$ region gives the same result: the charge is pulled away from the median plane

Wedge vertical focusing in the ZGS ($\epsilon > 0$) was at the expense of horizontal geometrical focusing (Fig. 9.7). This was an advantage though for the acceleration of polarized beams, as radial field components (which are responsible for depolarization) were only met at the EFBs of the eight main dipoles [12]. Preserving beam polarization at high energy required tight control of the tunes, and this was achieved by, in addition, pole face winding at the ends of the dipoles [15, 16]; these coils where pulsed to control amplitude detuning, resulting in tune control at 0.01 level, they also compensated eddy currents induced sextupole perturbations affecting the vertical tune.

Fringe field extent

The fringe field extent, say λ, may be taken into account in the thin lens approximation of the wedge focusing. It only modifies the horizontal focusing to the second order in the coordinates, but changes the vertical focusing to the first order, namely

$$\Delta \mathrm{x}' = \frac{\tan\epsilon}{\rho_0}\Delta \mathrm{x}, \quad \Delta \mathrm{y}' = -\frac{\tan(\epsilon - \psi)}{\rho_0}\Delta \mathrm{y} \tag{9.11}$$

wherein

$$\psi = \mathrm{I}_1 \frac{\lambda}{\rho_0}\frac{1+\sin^2\epsilon}{\cos\epsilon}, \quad \text{with } \mathrm{I}_1 = \int_{\mathrm{s(B=0)}}^{\mathrm{s(B=B_0)}} \frac{\mathrm{B(s)(B_0 - B(s))}}{\mathrm{B}_0^2}\frac{\mathrm{ds}}{\lambda} \tag{9.12}$$

and the integral I_1 extends over the field fall-off where B evolves between 0 to a plateau value B_0 inside the magnet.

Off-momentum orbits

In a dipole with field index $n = -\frac{\rho_0}{B_0}\frac{\partial B_y}{\partial \rho}$, concentric orbits with different momenta $p = p_0 + \Delta p$ (Fig. 9.7) are distant

$$\Delta x = \frac{\rho_0}{1-n}\frac{\Delta p}{p_0}$$

from the reference orbit at $p = p_0$ Given that $n < 1$,
- higher momentum orbits, $p > p_0$, have a greater radius,
- lower momentum orbits, $p < p_0$, have a smaller radius.

In a structure with axial symmetry, with drift sections (Fig. 9.8) or without (classical and AVF cyclotrons for instance), the ratio $\frac{\Delta x}{\rho_0\, dp/p_0} = \frac{1}{1-n}$ is independent of the azimuth s. Equilibrium trajectories enter and exit parallel to the optical axis of the bending dipoles. Introduce the geometrical radius $R = (1+k)\rho_0$ (Eq. 9.7) to account for the added drifts, the chromatic dispersion of the orbits thus amounts to

$$\frac{\Delta \mathrm{x}}{\Delta \mathrm{p}/\mathrm{p}_0} \equiv \frac{\Delta \mathrm{R}}{\Delta \mathrm{p}/\mathrm{p}_0} = \frac{\mathrm{R}}{(1-\mathrm{n})(1+\mathrm{k})} \tag{9.13}$$

Thus the dispersion function

$$D(s) = \frac{R}{(1-n)(1+k)} = D, \quad \text{constant} \tag{9.14}$$

is s-independent, the distance of a chromatic orbit to the reference orbit is constant around the ring.

Chromatic orbit length

In an axially symmetric structure the difference in closed orbit length $\Delta C = 2\pi\Delta R$ resulting from the difference in momentum arises in the dipoles, as all orbits are parallel in the drifts (Fig. 9.8). Hence, from Eq. 9.13, the relative closed orbit lengthening factor, "momentum compaction"

$$\alpha = \frac{\Delta C}{C} \Big/ \frac{\Delta \mathrm{p}}{\mathrm{p}_0} \equiv \frac{\Delta \mathrm{R}}{\mathrm{R}} \Big/ \frac{\Delta \mathrm{p}}{\mathrm{p}_0} = \frac{1}{(1-\mathrm{n})(1+\mathrm{k})} \approx \frac{1}{\nu_{\mathrm{x}}^2} \tag{9.15}$$

with $k = Nl/\pi\rho_0$ (Eq. 9.7). A note regarding the relationship $\alpha \approx 1/\nu_x^2$ between momentum compaction and horizontal wave number (it will be addressed quantitatively, below): this approximation was established in the case of a cylindrically symmetric structure, for which $\nu_x = \sqrt{1-n}$ (Eq. 4.19, 'Classical Cyclotron" Chapter). Adding short drifts such that $k \to 0$ (*i.e.*, $Nl \ll \pi\rho_0$), the relation still holds, thus leading to

$$\nu_x \approx \sqrt{(1-n)(1+k)} \approx \sqrt{(1-n)}(1+\frac{k}{2})$$

9.1.2 Betatron motion in a periodic structure, periodic stability

Equations of motion

The first order differential equations of motion in the Serret-Frénet frame (Fig. 9.8) derive from the Lorentz equation,

$$\frac{\mathrm{d}m\mathbf{v}}{\mathrm{dt}} = \mathrm{q}\mathbf{v}\times\mathbf{B} \;\Rightarrow\; \mathrm{m}\frac{\mathrm{d}}{\mathrm{dt}}\left\{\begin{matrix} \frac{ds}{dt}\mathbf{s} \\ \frac{dx}{dt}\mathbf{x} \\ \frac{dy}{dt}\mathbf{y} \end{matrix}\right\} = \mathrm{q}\left\{\begin{matrix} (\frac{dx}{dt}B_y - \frac{dy}{dt}B_x)\mathbf{s} \\ -\frac{ds}{dt}B_y\mathbf{x} \\ \frac{ds}{dt}B_x\mathbf{y} \end{matrix}\right\} \tag{9.16}$$

Introduce the field index $n = -\frac{\rho_0}{B_0}\frac{\partial B_y}{\partial x}$ evaluated on the reference orbit, with $B_0 = B_y(\rho_0, y=0)$; assume transverse stability: $0 < n < 1$. Taylor expansion of the field components in the moving frame write

$$B_y(\rho) = B_y(\rho_0) + x\frac{\partial B_y}{\partial x}\Big|_{\rho_0} + O(x^2) \approx B_y(\rho_0) - n\frac{B_y}{\rho_0}\Big|_{\rho_0} x = B_0(1 - n\frac{x}{\rho_0})$$

$$B_x(0+y) = \underbrace{B_x(0)}_{=0} + y\underbrace{\frac{\partial B_x}{\partial y}\Big|_{\rho_0}}_{=\frac{\partial B_y}{\partial x}} \text{(+ higher order in y)} \approx -n\frac{B_0}{\rho_0}y \tag{9.17}$$

Introduce in addition $ds \approx vdt$, Eqs. 9.16, 9.17 lead to the differential equations of motion in a dipole field

$$\frac{d^2x}{ds^2} + \frac{1-n}{\rho_0^2}x = 0, \quad \frac{d^2y}{ds^2} + \frac{n}{\rho_0^2}y = 0 \quad \left(0 < n = \frac{\rho_0}{B_0}\frac{\partial B_y}{\partial x} < 1\right) \tag{9.18}$$

It results that, in an S-periodic structure comprised of dipoles, wedges and drift spaces, the differential equation of motion takes the general form of Hill's equation, a second order differential equation with periodic coefficient, namely (with z standing for x or y),

$$\begin{cases} \dfrac{d^2z}{ds^2} + K_z(s)z = 0 \\ K_z(s+S) = K_z(s) \end{cases} \quad \text{with} \quad \begin{cases} \text{in dipoles : } \begin{cases} K_x = (1-n)/\rho_0^2 \\ K_y = n/\rho_0^2 \end{cases} \\ \text{at a wedge : } \mathrm{K}_{\substack{x\\y}} = \pm(\tan\epsilon)/\rho_0 \\ \text{in drift spaces : } \mathrm{K_x} = \mathrm{K_y} = 0 \end{cases} \tag{9.19}$$

$K_z(s)$ is S-periodic, $S = 2\pi R/N$ (S $= C/4$, for instance, in the 4-periodic ring Saturne 1 (Figs. 9.3, 9.8)). G. Floquet has established [17] that the two independent solutions of Hill's second order differential equation have the form

$$\left| \begin{array}{l} z_1(s) = \sqrt{\beta_z(s)}\, e^{i\int_0^s \frac{ds}{\beta_z(s)}} \\ dz_1(s)/ds = \dfrac{i-\alpha_z(s)}{\beta_z(s)}\, z_1(s) \end{array} \right. \quad \text{and} \quad \left| \begin{array}{l} z_2(s) = z_1^*(s) \\ dz_2(s)/ds = dz_1^*(s)/ds \end{array} \right. \tag{9.20}$$

wherein $\beta_z(s)$ and $\alpha_z(s) = -\beta_z'(s)/2$ are S-periodic functions, from what it results that

$$\mathrm{z}_{\substack{1\\2}}(\mathrm{s}+\mathrm{S}) = \mathrm{z}_{\substack{1\\2}}(\mathrm{s})\, \mathrm{e}^{\pm \mathrm{i}\mu_\mathrm{z}} \tag{9.21}$$

wherein

$$\mu_\mathrm{z} = \int_{\mathrm{s_0}}^{\mathrm{s_0+S}} \frac{\mathrm{ds}}{\beta_\mathrm{z}(\mathrm{s})} \tag{9.22}$$

is the betatron phase advance over a period. A real solution of Hill's equation is the linear combination $A\, z_1(s) \; + \; A^*\, z_2^*(s)$. Take A of the form $A = \frac{1}{2}\sqrt{\varepsilon/\pi}e^{i\phi}$ (the introduction of the constant multiplicative factor $\sqrt{\varepsilon/\pi}$ is justified below), the general solution of Eq. 9.19 then takes the form (noting $(*)$'=d(*)/ds)

$$\left| \begin{array}{l} z(s) = \sqrt{\beta_z(s)\varepsilon/\pi}\, \cos\left(\int \dfrac{ds}{\beta_z} + \phi\right) \\ z'(s) = -\sqrt{\dfrac{\varepsilon/\pi}{\beta_z(s)}}\, \sin\left(\int \dfrac{ds}{\beta_z} + \phi\right) + \alpha_z(s)\, \cos\left(\int \dfrac{ds}{\beta_z} + \phi\right) \end{array} \right. \tag{9.23}$$

The motion coordinates satisfy the following ellipse equation, Courant-Snyder invariant,

$$\frac{1}{\beta_z(s)}\left[z^2 + (\alpha_z(s)z + \beta_z(s)z')^2\right] = \frac{\varepsilon}{\pi} \tag{9.24}$$

At a given azimuth s of the periodic structure the observed turn-by-turn motion lies on that ellipse (Fig. 9.13). The form of the ellipse depends on the observation azimuth s via the respective local values of $\alpha_z(s)$ and $\beta_z(s)$, but its surface ε is invariant. Motion along the ellipse is clockwise, as can be figured from Eq. 9.23 considering an observation azimuth s where the ellipse is upright, $\alpha_z(s) = 0$.

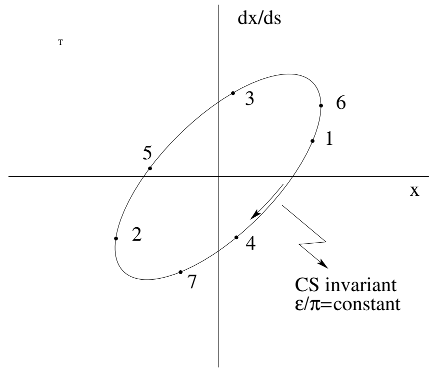

Fig. 9.13 Courant-Snyder invariant and turn-by-turn harmonic motion. The form of the ellipse depends on the observation azimuth s but its surface ε is invariant

If a turn is comprised of N periods, the phase advance over a turn (from one location to the next on the ellipse in Fig. 9.13) is

$$\int_{\mathrm{s_0}}^{\mathrm{s_0+NS}} \frac{\mathrm{ds}}{\beta_\mathrm{z}(\mathrm{s})} = \mathrm{N} \int_{\mathrm{s_0}}^{\mathrm{s_0+S}} \frac{\mathrm{ds}}{\beta_\mathrm{z}(\mathrm{s})} = \mathrm{N}\mu_\mathrm{z} \tag{9.25}$$

Weak focusing approximation

In the case of a cylindrically symmetric structure, a sinusoidal motion (Eqs. 4.13, 4.14, "Classical Cyclotron" Chapter) is the exact solution of the first order differential equations of motion. In that case the latter have a constant (s-independent) coefficient, $K_x = (1-n)/R_0^2$ and $K_y = n/R_0^2$, respectively. Adding drift spaces results in Hill's differential equation with periodic coefficient $K(s+S) = K(s)$ (Eq. 9.19) and to a pseudo harmonic solution (Eq. 9.23). Due to the weak focusing the beam envelope (Eq. 9.30) is only weakly modulated, thus so is $\beta_z(s)$. In a practical manner, the modulation of $\beta_z(s)$ does not exceed a few percent, this justifies introducing the average value $\overline{\beta}_z$ to approximate the phase advance by

$$\int_0^s \frac{ds}{\beta_z(s)} \approx \frac{s}{\overline{\beta}_z} = \nu_z \frac{s}{R}$$

The right equality is obtained by applying this approximation to the the phase advance per period (Eq. 9.32), namely $\mu_z = \int_{s_0}^{s_0+S} \dfrac{ds}{\beta_z(s)} \approx S/\overline{\beta_z}$, and introducing the wave number of the N-period optical structure

$$\nu_z = \frac{N\mu_z}{2\pi} = \frac{\text{phase advance over a turn}}{2\pi} \tag{9.26}$$

so that

$$\overline{\beta_z} = \frac{R}{\nu_z} \tag{9.27}$$

Substituting in Eq. 9.23 results in the approximate solution

$$\left|\begin{array}{l} z(s) \approx \sqrt{\beta_z(s)\varepsilon/\pi}\, \cos\left(\nu_z \frac{s}{R} + \phi\right) \\ z'(s) = -\sqrt{\frac{\varepsilon/\pi}{\beta_z(s)}}\, \sin\left(\nu_z \frac{s}{R} + \phi\right) + \alpha_z(s)\, \cos\left(\nu_z \frac{s}{R} + \phi\right) \end{array}\right. \tag{9.28}$$

In this approximation, the differential equations of motion (Eq. 9.19) can be expressed under the form

$$\frac{d^2x}{ds^2} + \frac{\nu_x^2}{R^2}x = 0, \qquad \frac{d^2y}{ds^2} + \frac{\nu_y^2}{R^2}y = 0 \tag{9.29}$$

Beam envelopes

The beam envelope $\hat{z}(s)$ (with z standing for x or y) is determined by the particle of maximum invariant ε/π, it is given by

$$\pm\hat{z}(s) = \pm\sqrt{\beta_z(s)\varepsilon/\pi} \tag{9.30}$$

As $\beta_z(s)$ is S-periodic, so is the envelope, $\hat{z}(s + S) = \hat{z}(s)$. In a cell with symmetries

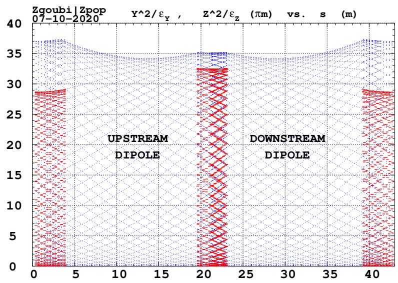

Fig. 9.14 ********* remplace par envelope in saturne1 ********* Beam envelope along Saturne I four cells, generated by a single particle over many turns. The extreme excursion at any azimuth s tangents the envelope. Envelopes along a cell feature central symmetry, as does the cell

(for instance symmetry with respect to the center of the cell), the envelope features the same symmetries. Envelope extrema are at azimuth s where $\beta_z(s)$ is minimum, or maximum, *i.e.*, where $\alpha_z = 0$ as $\beta_z' = -2\alpha_z$. This is illustrated in Fig. 9.14. No particular hypothesis regarding the amplitude of the motion is required here, it does not have to be paraxial and can be arbitrarily large (as long as transverse stability still holds).

In the paraxial approximation, envelopes along the optical structure can be determined by resorting to matrix transport (*cf.* reminders in Section 19.3.2). An initial beam matrix at some azimuth s, as well as the phase advance over a period, can be obtained using the stability criterion (Eq. 19.3.3). This is a simple exercise in the case of Saturne I type of structure (Figs. 9.3, 9.8). The transport matrix of the symmetric drift-dipole-drift cell satisfies

$$[T_{\mathrm{per.}}] = \begin{bmatrix} 1 & l \\ 0 & 1 \end{bmatrix} \begin{bmatrix} \cos(\sqrt{K_z}\rho_0\alpha) & \frac{1}{\sqrt{K_z}}\sin(\sqrt{K_z}\rho_0\alpha) \\ -\sqrt{K_z}\sin(\sqrt{K_z}\rho_0\alpha) & \cos(\sqrt{K_z}\rho_0\alpha) \end{bmatrix} \begin{bmatrix} 1 & l \\ 0 & 1 \end{bmatrix}$$
$$= \begin{bmatrix} \cos(\sqrt{K_z}\rho_0\alpha) - \sqrt{K_z}l\sin(\sqrt{K_z}\rho_0\alpha) & 2l\cos(\sqrt{K_z}\rho_0\alpha) + \frac{1}{\sqrt{K_z}}\sin(\sqrt{K_z}\rho_0\alpha)(1-K_z l^2) \\ -\sqrt{K_z}\sin(\sqrt{K_z}\rho_0\alpha) & \cos(\sqrt{K_z}\rho_0\alpha) - \sqrt{K_z}l\sin(\sqrt{K_z}\rho_0\alpha) \end{bmatrix}$$
$$\approx \begin{bmatrix} \cos\sqrt{K_z}(\rho_0\alpha + l) & 2l\cos(\sqrt{K_z}\rho_0\alpha) + \frac{1}{\sqrt{K_z}}\sin(\sqrt{K_z}\rho_0\alpha) \\ -\sqrt{K_z}\sin(\sqrt{K_z}\rho_0\alpha) & \cos\sqrt{K_z}(\rho_0\alpha + l) \end{bmatrix} \tag{9.31}$$

The approximation is obtained by assuming that the drift length $2l$ is small compared to the arc length $\rho_0\alpha$. From the stability criterion $[T_{\mathrm{per.}}] = I\cos\mu_z + J\sin\mu_z$ it results that $\frac{1}{2}\mathrm{Tr}[\mathrm{T}_{\mathrm{per.}}] = \cos\mu_z$, which yields the phase advance

$$\mu_z = \sqrt{\mathrm{K_z}}(\rho_0\alpha + \mathrm{l}) = \sqrt{\mathrm{K_z}}\rho_0\alpha(1 + \mathrm{k}/2) \tag{9.32}$$

With $\nu_z = N\mu_z/2\pi$ and (Eq. 9.19) $K_x = (1-n)/\rho_0^2$, $K_y = n/\rho_0^2$, $N\alpha = 2\pi$, $k = 2l/\rho_0\alpha \ll 1$, this yields for the horizontal and vertical tunes

$$\nu_x \approx \sqrt{1-\mathrm{n}}(1 + \frac{\mathrm{k}}{2}) \approx \sqrt{(1-\mathrm{n})\frac{\mathrm{R}}{\rho_0}}, \qquad \nu_y \approx \sqrt{\mathrm{n}}(1 + \frac{\mathrm{k}}{2}) \approx \sqrt{\mathrm{n}\frac{\mathrm{R}}{\rho_0}} \tag{9.33}$$

The identification $[T_{\mathrm{per.}}] = I\cos\mu_z + J\sin\mu_z$ allows writing $[T_{\mathrm{per.}}]$ under the form

$$[T_{\mathrm{per.}}] = \begin{bmatrix} \cos\sqrt{K_z}(\rho_0\alpha + l) & \frac{1+\sqrt{K_z}l\cot(\sqrt{K_z}\rho_0\alpha)}{\sqrt{K_z}}\sin\sqrt{K_z}(\rho_0\alpha + l) \\ -\frac{\sqrt{K_z}}{1+\sqrt{K_z}l\cot(\sqrt{K_z}\rho_0\alpha)}\sin\sqrt{K_z}(\rho_0\alpha + l) & \cos\sqrt{K_z}(\rho_0\alpha + l) \end{bmatrix} \tag{9.34}$$

so leading to the optical functions at the center of the drift,

$$\alpha_z = 0, \qquad \beta_z = \frac{1}{\sqrt{K_z}}\left[1 + \sqrt{K_z}l\cot(\sqrt{K_z}\rho_0\alpha)\right] \tag{9.35}$$

Stability diagram

The "working point" of the synchrotron is the couple (ν_x, ν_y) at which the accelerator is operated, it fully characterizes the focusing. In a structure with cylindrical symmetry (*cf.* Eq. 4.15) $\nu_x = \sqrt{1-n}$ and $\nu_y = \sqrt{n}$ so that $\nu_x^2 + \nu_y^2 = 1$: when the radial field index n is changed the working point stays on a circle of radius 1 in the stability diagram (or "tune diagram", Fig. 9.15). If drift spaces are added, in a first

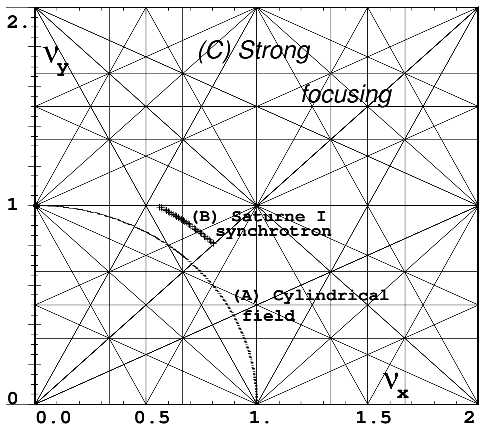

Fig. 9.15 Location of the working point in the tune diagram, in case of (A) field with revolution symmetry, on a circle of radius 1; (B) sector field with index + drift spaces, on a circle of radius ($\sqrt{R/\rho_0}$); (C) strong focusing, ($|n| \gg 1$), in large ν_x, ν_y regions.

approximation (Eq. 9.33)

$$\nu_\mathrm{x} = \sqrt{(1-\mathrm{n})\frac{\mathrm{R}}{\rho_0}}, \quad \nu_\mathrm{y} = \sqrt{\mathrm{n}\frac{\mathrm{R}}{\rho_0}}, \qquad \nu_\mathrm{x}^2 + \nu_\mathrm{y}^2 = \frac{\mathrm{R}}{\rho_0} \tag{9.36}$$

the working point is located on the circle of radius $\sqrt{R/\rho_0} > 1$.

Horizontal and vertical focusing are not independent: if ν_x increases then ν_y decreases and reciprocally; none can exceed the limits

$$0 < \nu_\mathrm{x,\,y} < \sqrt{R/\rho_0}$$

This is a lack of flexibility which strong focusing will overcome by providing two knobs so allowing adjustment of both tunes separately.

9.1.3 Longitudinal Motion

Acceleration of the Ideal Particle

In a synchrotron, the field B is varied (a function performed by the power supply) as well as the bunch momentum p (a function performed by the accelerating cavity) in such a way that at any time $B(t)\rho = p(t)/q$ (ρ is the curvature radius of the central trajectory in the bending magnets). If this condition is fulfilled, then at all times during the acceleration cycle the central trajectory remains on the design optical axis, which is comprised of the reference arc in the dipoles, of the axis of the vacuum pipe in the straight section, of the accelerating cavities, of the beam position monitors, etc. Given the energies involved, the magnet supply imposes its law and the cavity follows $B(t)$, the best in can. A schematic B(t) law is represented in Fig. 9.16.

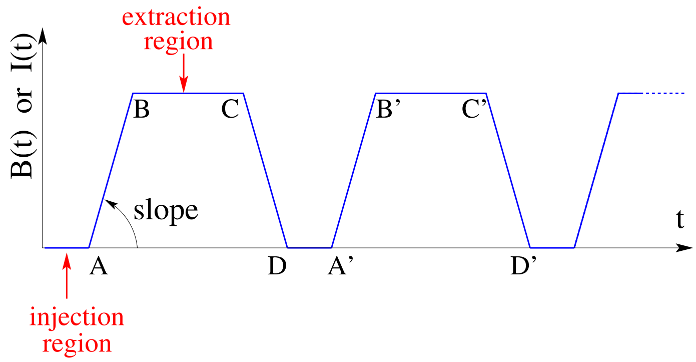

Fig. 9.16 Cycling $B(t)$ in a pulsed synchrotron. Ignoring saturation, $B(t)$ is proportional to the magnet power supply current $I(t)$. Bunch injection occurs at low field, in the region of A, extraction occurs at top energy, on the high field plateau. (AB): field ramp up (acceleration); (BC): flat top (includes beam extraction period); (CD): field ramp down; (DA'): thermal relaxation. (AA'): repetition period; (1/AA'): repetition rate; *slope*: ramp velocity $\dot{B} = dB/dt$ (Tesla/s).

Typical values from Saturne I synchrotron are given in Tab. 9.1. As the central

Table 9.1 Saturne I field parameters

$\dot{B}$	1.8 T/s
B_{max}	1.5 T
ρ	8.42 m
$B_{max}\rho$	13 T m

trajectory length is fixed ($2\pi R \approx 68.9$ m, see Tab. 9.2) whereas particle velocity increases turn after turn, thus the revolution time T_{rev} varies.

$$\mathrm{T_{rev}} = \frac{\text{duration of a turn}}{\text{velocity}} = \frac{2\pi \mathrm{R}}{\beta \mathrm{c}}$$

$$\mathrm{R}_{\mathrm{Sat.I}} = 10.97\,\mathrm{m}, \left| \begin{array}{l} \text{initial E} = 3.6\,\mathrm{MeV} \\ \text{final E} = 2.94\,\mathrm{GeV} \end{array} \right. \Rightarrow \left| \begin{array}{l} \mathrm{T}_{\mathrm{rev}} = \frac{2\pi \mathrm{R}}{0.09\times 3\,10^8} = 16.5\,\mu\mathrm{s};\ \mathrm{f} = 0.06.\,\mathrm{MHz} \\ \mathrm{T}_{\mathrm{rev}} = \frac{2\pi \mathrm{R}}{0.97\times 3\,10^8} = 0.24\,\mu\mathrm{s};\ \mathrm{f} = 4.2\,\mathrm{MHz} \end{array} \right.$$

The accelerating voltage $\hat{V}(t) = \sin \omega_{\mathrm{rf}} t$ is maintained in synchronism with the revolution motion, thus its angular frequency ω_{rf} follows $h f_{\mathrm{rev}}$,

$$\omega_{\mathrm{rf}} = h\omega_{\mathrm{rev}} = h\frac{c}{R}\frac{B(t)}{\sqrt{\left(\frac{m_0}{q\rho}\right)^2 + B^2(t)}}$$

Energy gain

The variation of the particle energy over a turn amounts to the work of the force $F = dp/dt$ on the charge at the cavity, namely

$$\Delta W = F \times 2\pi R = 2\pi q R \rho \dot{B} \tag{9.37}$$

Over most of the acceleration cycle in a slow-cycling synchrotron $\dot{B}$ is usually constant (Eq. 9.3), thus so is ΔW. At Saturne I for instance

$$\frac{\Delta W}{q} = 2\pi R \rho \dot{B} = 68.9 \times 8.42 \times 1.8 = 1044\,\text{volts}$$

The field ramp lasts

$$\Delta t = (B_{\mathrm{max}} - B_{\mathrm{min}})/\dot{B} \approx B_{\mathrm{max}}/\dot{B} = 0.8\,\mathrm{s}$$

The number of turns to the top energy ($W_{\mathrm{max}} \approx 3\,\mathrm{GeV}$) is

$$N = \frac{W_{\mathrm{max}}}{\Delta W} = \frac{3\,10^9\ \mathrm{eV}}{1044\ \mathrm{eV}} \approx 3\,10^6$$

Adiabatic damping of betatron oscillations

During acceleration, focusing strengths follow the increase of particle rigidity, so to maintain the tunes ν_x and ν_y constant. As a result of the longitudinal acceleration at the cavity though, the longitudinal energy of the particles is modified. This results in a decrease of the amplitude of betatron oscillations (an increase if the cavity is decelerating). The mechanism is sketched in Fig. 9.17: the slope, respectively before (index 1) and after (index 2) the cavity is

$$\frac{dx}{ds} = \frac{m\frac{dx}{dt}}{m\frac{ds}{dt}} = \frac{p_x}{p_s}, \qquad \left.\frac{dx}{ds}\right|_2 = \left.\frac{m\frac{dx}{dt}}{m\frac{ds}{dt}}\right|_2 = \frac{p_{x,2}}{p_{s,2}}$$

Particle mass and velocity are modified at the traversal of the cavity but, as the

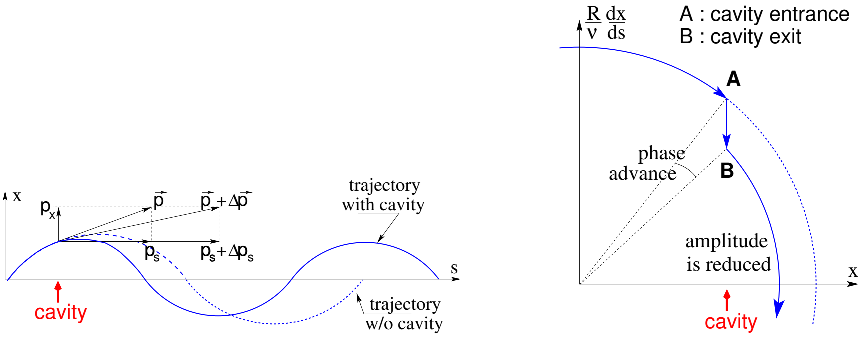

Fig. 9.17 Adiabatic damping of betatron oscillations, here from $x' = p_x/p_s$ before the cavity, to $x'_2 = p_x/(p_s + \Delta p_s)$ after the cavity. In the horizontal phase space, to the right, decrease of $\Delta\left(\frac{dx}{ds}\right)$ if $\frac{dx}{ds} > 0$, increase of $\Delta\left(\frac{dx}{ds}\right)$ if $\frac{dx}{ds} < 0$

force is longitudinal, $dp_x/dt = 0$ thus $p'_x = p_x$, the increase in momentum is purely longitudinal, $p'_s = p_s + \Delta p$. Thus

$$\left.\frac{dx}{ds}\right|_2 = \frac{p_x}{p_s + \Delta p} \approx \frac{p_x}{p_s}(1 - \frac{\Delta p}{p_s})$$

and as a consequence the slope dx/ds varies across the cavity,

$$\Delta\left(\frac{dx}{ds}\right) = \left.\frac{dx}{ds}\right|_2 - \frac{dx}{ds} = -\frac{dx}{ds}\frac{\Delta p_s}{p_s}$$

The slope varies in proportion to the slope, with opposite sign if $\Delta p/p > 0$ (acceleration) thus a decrease of the slope. This variation has two consequences on the betatron oscillation (Fig. 9.17):

- a change of the betatron phase,
- a modification of the betatron amplitude.

In matrix form

Coordinate transport through the cavity writes $\begin{cases} x_2 = x \\ x'_2 \approx \frac{p_x}{p_s}(1 - \frac{dp}{p}) = x'(1 - \frac{dp}{p}) \end{cases}$, hence the transfer matrix of the cavity,

$$[\mathrm{C}] = \begin{bmatrix} 1 & 0 \\ 0 & 1 - \frac{dp}{p} \end{bmatrix} \tag{9.38}$$

its determinant is $1 - dp/p \neq 1$: the system is non-conservative (the surface in phase space is not conserved). Assume one cavity in the ring and not $[T]\times[C]$ the one-turn matrix with origin at entrance of the cavity. Its determinant is $det[T] \times det[C] = det[C] = 1 - \frac{dp}{p}$. Over N turns the coordinate transport matrix is $([T][C])^N$, its determinant is $(1 - \frac{dp}{p})^N \approx 1 - N\frac{dp}{p}$. The surface of the beam ellipse is $\varepsilon \times det[T]_{turn} = \varepsilon_0 - \varepsilon\frac{dp}{p}$ thus $\frac{d\varepsilon}{\varepsilon} = -\frac{dp}{p}$, the solution of which is

$$\varepsilon \times \mathrm{p} = \text{constant}, \quad \text{or} \quad \beta\gamma\varepsilon = \text{constant} \tag{9.39}$$

Synchrotron motion; the synchronous particle

By "synchrotron motion", or "phase oscillations", it is meant a mechanism that stabilizes the longitudinal motion of a particle around a synchronous phase, in virtue of

(i) the presence of an accelerating cavity with its frequency indexed on the revolution time,

(ii) with the bunch centroid positioned either on the rising slope of the oscillating voltage (low energy regime), or on the falling slope (high energy regime).

The synchronous (or "ideal") particle follows the equilibrium trajectory around the ring (the reference closed orbit, about which all other particles will undergo a betatron oscillation) and its velocity satisfies

$$B\rho = \frac{p}{q} = \frac{mv}{p} \longrightarrow v = \frac{qB\rho}{m}$$

- the revolution time is $T_{rev} = \frac{2\pi R}{v} = \frac{2\pi R}{\beta c} = \frac{2\pi R}{qB\rho/m}$
- the angular revolution frequency follows the increase of B:

$$\omega_{rev} = \frac{2\pi}{T_{rev}} = \frac{qB\rho}{mR}$$

- during the acceleration $B(t)$ increases at a $\frac{dB}{dt} = \dot{B}$ rate normally of the order of a Tesla/second.
- in order for the ideal particle to stay on the closed orbit during the acceleration, its changing momentum must at all time satisfy $B(t)\rho = p(t)/q$. This defines $p(t)$ as a function of $B(t)$, and the following B dependence of mass and angular frequency:

$$m(t) = \gamma(t)m_0 = \frac{q\rho}{c}\sqrt{\left(\frac{m_0}{qc\rho}\right)^2 + B(t)^2}$$

$$\omega_{rev}(t) = \frac{c}{R}\frac{B(t)}{\sqrt{\left(\frac{m_0}{qc\rho}\right)^2 + B(t)^2}}$$

- the RF voltage frequency $\omega_{RF}(t) = h\omega_{rev}(t)$ follows B(t), this maintains the synchronous phase at a fixed value
- over a turn the gain in energy is $\Delta W = 2\pi q R \rho \dot{B}$, the reference particle experiences a voltage $V = \Delta W/q = 2\pi R \rho \dot{B}$.

Simulation wise, the ramping of the guide field can be assumed to follow a step function in correlation with the step increase of particle momentum at the RF cavity. In that manner, the synchronous particle is maintained on the design orbit, at radius $\rho = p(t)/qB(t)$=constant in the guide magnets.

Phase Stability

The mechanism of phase stability has, first experimented in the synchrocyclotron [18] has been introduced in the eponym Chapter (Chap. 8). It is re-visited here accounting for specificities of the operation of a synchrotron, such as the constant radius orbit, or the concept of transition energy.

Note ϕ_s the RF phase at arrival of the synchronous particle at the aforementioned accelerating cavity, its energy gain is

$$\Delta W = q\hat{V} \sin \phi_s = 2\pi q R \rho \dot{B}$$

The condition $|\sin \phi_s| < 1$ imposes a lower limit to the cavity voltage for acceleration to happen, namely

$$\hat{V} > 2\pi R \rho \dot{B}$$

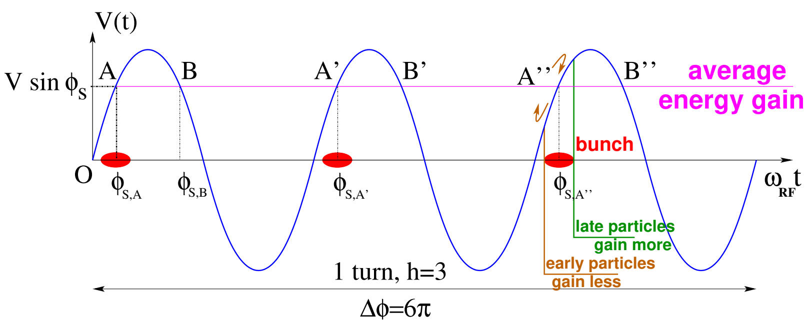

Fig. 9.18 Mechanism of phase stability, "longitudinal focusing". Below transition ($\gamma < \gamma_{tr}$) phase stability occurs for a synchronous phase taken at either of the h=3 stable locations A, A', A": a particle with higher energy goes around the ring more rapidly than the synchronous particle, it arrives earlier at the voltage gap (at $\phi < \phi_{s,A}$) and experiences a lower voltage; at lower energy the particle is slower, it arrives at the gap later compared to the synchronous particle, at $\phi > \phi_{s,A}$, and experiences a greater voltage; this results overall in a stable oscillatory motion around the synchronous phase. Beyond transition ($\gamma > \gamma_{tr}$) the stable phase is at either of the h=3 stable locations B, B', B':, a particle which is less energetic than the synchronous particle arrives earlier, $\phi < \phi_{s,B}$, it experiences a greater voltage, and inversely when it eventually gets more energetic than the synchronous particle

Referring to Fig. 9.18, the synchronous phase can be placed on the left (A A' A"... series in the Figure, or on the right (B B' B"... series) of the oscillating voltage crest. One and only one of these two possibilities, and which one depends on the optical lattice and on particle energy, ensures that particles in a bunch remain grouped in the vicinity of the synchronous particles. The transition between these two regimes (A series or B series) occurs at the transition γ, γ_{tr}, a property of the lattice. If the bunch energy is below transition energy, $E_{\mathrm{bunch}} < m\gamma_{\mathrm{tr}}$, the bunch has to present itself on the left of the crest (A series), if the bunch energy is greater than transition energy, $E_{\mathrm{bunch}} > m\gamma_{\mathrm{tr}}$, the bunch has to present itself on the right of the crest (B series).

Transition energy

The transition between the two regimes occurs at $\dfrac{dT_{\mathrm{rev}}}{T_{\mathrm{rev}}} = 0$. With $T = 2\pi/\omega = C/v$, this can be written $\dfrac{d\omega_{\mathrm{rev}}}{\omega_{\mathrm{rev}}} = -\dfrac{dT_{\mathrm{rev}}}{T_{\mathrm{rev}}} = \dfrac{dv}{v} - \dfrac{dC}{C}$. With $\frac{dv}{v} = \frac{1}{\gamma^2}\frac{dp}{p}$ and momentum compaction $\alpha = \dfrac{dC}{C} \,/\, \frac{dp}{p}$, (Eq. 9.15), this can be written

$$\frac{\mathrm{d}\omega_{\mathrm{rev}}}{\omega_{\mathrm{rev}}} = -\frac{\mathrm{dT_{rev}}}{\mathrm{T_{rev}}} = (\frac{1}{\gamma^2} - \alpha)\frac{\mathrm{dp}}{\mathrm{p}} = \eta\frac{\mathrm{dp}}{\mathrm{p}} \tag{9.40}$$

wherein the phase-slip factor has been introduced,

$$\eta = \overbrace{\frac{1}{\gamma^2}}^{\text{kinematics}} - \underbrace{\alpha}_{\text{lattice}} \tag{9.41}$$

In a weak focusing structure $\alpha \approx 1/\nu_x^2$ (Eqs. 4.19, 9.15), thus the phase stability regime is

$$\text{below transition, } \textit{i.e. } \phi_{\mathrm{s}} < \pi/2, \quad \text{if} \quad \gamma < \nu_{\mathrm{x}} \tag{9.42}$$

$$\text{above transition, } \textit{i.e.} \phi_{\mathrm{s}} > \pi/2, \quad \text{if} \quad \gamma > \nu_{\mathrm{x}} \tag{9.43}$$

(9.44)

In weak focusing synchrotrons the horizontal tune $\nu_x = \sqrt{(1-n)R/\rho_0}$ (Eq. 9.33) may be $\gtrless 1$, and subsequently $\gamma_{\mathrm{tr}} \approx \nu_x \gtrless 1$ depending on the horizontal tune value. Saturne I for instance, with $\nu_x \approx 0.7$ (Tab. 9.2), operated above transition energy.

9.1.4 Spin Motion, Depolarizing Resonances

The availability of polarized proton sources allowed the acceleration of polarized beams to high energy. The possibility was considered from the early times of the ZGS [19], up to 70% polarization transmission through the synchrotron was foreseen, polarization manipulation concepts included harmonic orbit correction, tune jump at strongest depolarizing resonances (Fig. 9.19). Acceleration of a polarized proton beam happened for the first time in a synchrotron and to multi-GeV energy in 1973, four years after the ZGS startup. Beams were accelerated up to 17 GeV with substantial polarization maintained [12]. Experiments were performed to assess the possibility of polarization transmission in strong focusing synchrotrons, and polarization lifetime in colliders [20]. Acceleration of polarized deuteron was achieved in the late 1970s, when sources where made available [21].

The field index is essentially zero in the ZGS, transverse focusing is ensured by wedge angles at the ends of the height dipoles, which is thus the only location where non-zero horizontal field components are found. The vertical wave number is small in addition, less than 1. This results in depolarizing resonance strengths on the weak side, *"As we can see from the table, the transition probability [from spin state $\psi_{1/2}$ to spin state $\psi_{-1/2}$] is reasonably small up to $\gamma = 7.1$"* [12], *i.e.* $G\gamma = 12.73$, $p = 6.6$ GeV/c; the table referred to stipulates a transition probability $P_{\frac{1}{2},-\frac{1}{2}} < 0.042$, whereas resonances beyond that energy range feature $P_{\frac{1}{2},-\frac{1}{2}} > 0.36$. Beam depolarization up to 6 GeV/c, under the effect of these resonances, is illustrated in Fig. 9.19.

In weak focusing synchrotron particles experience radial fields all along the bend dipoles as an effect of the radial field index, as they undergo vertical betatron oscillations. However these radial field components are weak, and so is there effect on spin motion, as long as the particle energy (the γ factor in the spin precession equation) is not too high.

Assuming a defect-free ring, the vertical betatron motion excites "intrinsic" spin resonances, located at

$$G\gamma_R = k\,P \pm \nu_y$$

with k an integer and P the period of the ring. In the ZGS for instance, $\nu_y \approx 0.8$ (Tab. 9.3), the ring P=4-periodic, thus $G\gamma_R = 4k \pm 0.8$. Strongest resonances are located at

$$G\gamma_R = MP\,k \pm \nu_y$$

with M the number of cells per superperiod [22, Sec. 3.II]. In the ZGS, M=2 thus strongest resonances occur at $G\gamma_R = 2 \times 4k \pm 0.8$.

In the presence of vertical orbit defects, non-zero periodic transverse fields are experienced along the closed orbit, they excite "imperfection" depolarizing resonances, located at

$$G\gamma_R = k$$

with k an integer. In the case of systematic defects the periodicity of the orbit is that of the lattice, P, imperfection resonances are located at $G\gamma_R =$ kP. Strongest

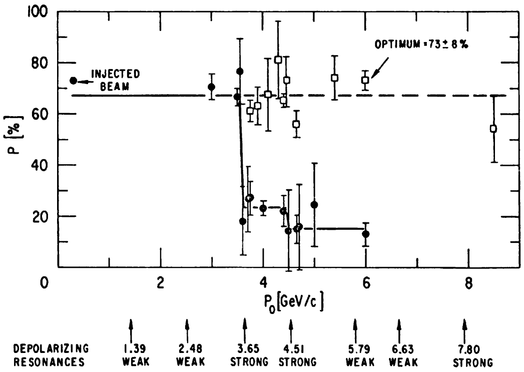

Fig. 9.19 Depolarizing intrinsic resonance landscape up to 6 GeV/c at the ZGS (solid circles). Systematic resonances are located at $G\gamma_R$ = 4×integer±ν_y, stronger ones at $G\gamma_R = 8 \times \text{integer} \pm \nu_y$. Tune jump was used to preserve polarization when crossing strong resonances (empty circles) [23]

imperfection resonances are located at

$$G\gamma_R = MP\,k$$

with M the number of cells per superperiod [22, Sec. 3.II]. Crossing a depolarizing resonance, during acceleration, causes a loss of polarization given by (Froissart-Stora formula [11])

$$\frac{\mathrm{P_f}}{\mathrm{P_i}} = 2\mathrm{e}^{-\frac{\pi}{2}\frac{|\epsilon_R|^2}{\alpha}} - 1 \tag{9.45}$$

from a value P_i upstream to an asymptotic value P_f downstream of the resonance. This assumes an isolated resonance, passed with a crossing speed

$$\alpha = \mathrm{G}\frac{\mathrm{d}\gamma}{\mathrm{d}\theta} = \frac{1}{2\pi}\frac{\Delta \mathrm{E}}{\mathrm{M}} \tag{9.46}$$

with ΔE the energy gain per turn and M the mass. ϵ_R is the resonance strength.

Spin precession axis. Resonance width

Consider the spin vector $\mathbf{S}(\theta) = (S_\eta, S_\xi, S_y)$ of a particle in the laboratory frame, with θ the orbital angle around the accelerator. Introduce the projection $s(\theta)$ of $\mathbf{S}$ in the median plane

$$s(\theta) = S_\eta(\theta) + jS_\xi(\theta) \qquad (\text{and } S_y^2 = 1 - s^2) \tag{9.47}$$

It can be shown that in the case of a stationary solution of the spin motion (*i.e.*, the spin precession axis) s satisfies [24] (Fig. 9.20)

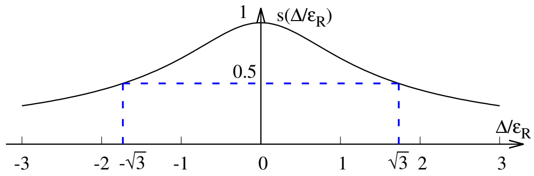

Fig. 9.20 Modulus of the horizontal spin component. $s = 1/2$ at distance $\Delta = \pm\sqrt{3}\epsilon_R$ from $G\gamma_R$

$$s^2 = \frac{1}{1 + \dfrac{\Delta^2}{|\epsilon_R|^2}} \tag{9.48}$$

wherein $\Delta = G\gamma - G\gamma_R$ is the distance to the resonance. The resonance width is a

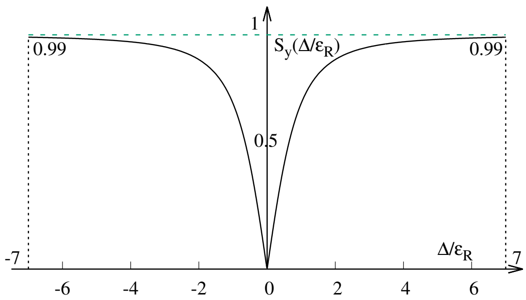

Fig. 9.21 Dependence of polarization on the distance to the resonance. For instance $S_y = 0.99$, 1% depolarization, corresponds to $\Delta = 7|\epsilon_R|$. On the resonance, $\Delta = 0$, the precession axis lies in the median plane, $S_y = 0$

measure of its strength (Fig. 9.21). The quantity of interest is the angle, ϕ, of the spin precession direction to the vertical axis, given by (Fig. 9.21)

$$\cos\phi(\Delta) \equiv S_y(\Delta) = \sqrt{1 - s^2} = \frac{\Delta/|\epsilon_R|}{\sqrt{1 + \Delta^2/|\epsilon_R|^2}} \tag{9.49}$$

On the resonance, $\Delta = 0$, the spin precession axis lies in the bend plane: $\phi = \pm\pi/2$. $S_y = 0.99$ (1% depolarization) corresponds to a distance to the resonance $\Delta = 7|\epsilon_R|$, and spin precession axis at an angle $\phi = \mathrm{acos}(0.99) = 8^{\circ}$ from the vertical.

Conversely,

$$\frac{\Delta^2}{|\epsilon_R|^2} = \frac{S_y^2}{1 - S_y^2} \tag{9.50}$$

The precession axis is common to all spins, S_y is a measure of the polarization along the vertical axis,

$$S_y = \frac{N^+ - N^-}{N^+ + N^-}$$

wherein N^+ and N^- denote the number of particles in spin states $\frac{1}{2}$ and $-\frac{1}{2}$ respectively.

Spin motion through weak resonances

Depolarizing resonances are weak up to several GeV in a weak focusing synchrotron, as the radial and/or longitudinal fields, which stem from a small radial field index and from dipole fringe fields, are weak. Spin motion $S_y(\theta)$ through a resonance in that case (*i.e.*, assuming $S_{y,f} \approx S_{y,i}$, with $S_{y,f}$ and $S_{y,i}$ the asymptotic vertical spin component values respectively upstream and downstream of the resonance) can be calculated in terms of the Fresnel integrals

$$C(x) = \int_0^x \cos\left(\frac{\pi}{2}t^2\right)\,dt, \qquad S(x) = \int_0^x \sin\left(\frac{\pi}{2}t^2\right)\,dt$$

namely, with the origin of the orbital angle taken at the resonance [24] (Fig. 9.22)

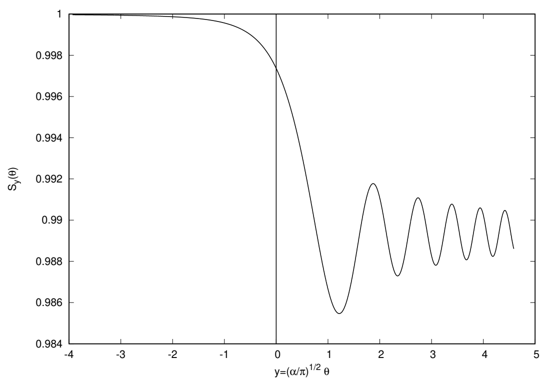

Fig. 9.22 Vertical component of spin motion $S_y(\theta)$ through a weak depolarizing resonance (after Eq. 9.51). The vertical bar is at the location of the resonance, which coincides with the origin of the orbital angle

$$\text{if } \theta < 0: \ \left(\frac{\mathrm{S_y}(\theta)}{\mathrm{S_{y,i}}}\right)^2 = 1 - \frac{\pi}{\alpha}|\epsilon_\mathrm{R}|^2 \left\{\left[0.5 - \mathrm{C}\left(-\theta\sqrt{\frac{\alpha}{\pi}}\right)\right]^2 + \left[0.5 - \mathrm{S}\left(-\theta\sqrt{\frac{\alpha}{\pi}}\right)\right]^2\right\}$$

$$\text{if } \theta > 0: \ \left(\frac{\mathrm{S_y}(\theta)}{\mathrm{S_{y,i}}}\right)^2 = 1 - \frac{\pi}{\alpha}|\epsilon_\mathrm{R}|^2 \left\{\left[0.5 + \mathrm{C}\left(\theta\sqrt{\frac{\alpha}{\pi}}\right)\right]^2 + \left[0.5 + \mathrm{S}\left(\theta\sqrt{\frac{\alpha}{\pi}}\right)\right]^2\right\} \quad (9.51)$$

In the asymptotic limit,

$$\frac{S_y(\theta)}{S_{y,i}} \xrightarrow{\theta\to\infty} 1 - \frac{\pi}{\alpha}|\epsilon_R|^2 \quad (9.52)$$

which identifies with the development of Froissart-Stora formula $P_f/P_i = 2\exp(-\frac{\pi}{2}\frac{|\epsilon_R|^2}{\alpha})-1$, to first order in $|\epsilon_R|^2/\alpha$. This approximation holds in the limit that higher order terms can be neglected, *viz.* $|\epsilon_R|^2/\alpha \ll 1$.

9.2 Exercises

9.1 Construct Saturne I synchrotron. Spin Resonances

Solution: page 346

In this exercise, Saturne I synchrotron is modeled in `zgoubi`, and spin resonances in a weak focusing gradient synchrotron are studied.

(a) Construct a model of the Saturne I synchrotron, using DIPOLE. Use Fig. 9.23 as a guidance, and parameters given in Tab. 9.2. Assume that the reference orbit is the same at all energies, on nominal radius, 841.93 cm. It is judicious (although in no way an obligation) to take RM=841.93 in DIPOLE.

Check the correctness of the model by producing the lattice parameters of the ring. TWISS can be used for that. Compare with the lattice parameters given in Tab. 9.2.

Produce a tune scan of the wave numbers over the radial field index $0.5 \leq n \leq 0.757$ operation range. The REBELOTE do loop can be used for that, to repeatedly change n and compute a MATRIX. Compare with theoretical expectations.

(b) Produce a graph of the betatron functions along the Saturne I cell. Provide checks of the correctness of the computation.

Check the theoretical periodic dispersion (Eq. 9.14) against the radial distance between on- and off-momentum closed orbits obtained from tracking. Provide a plot of the dispersion function.

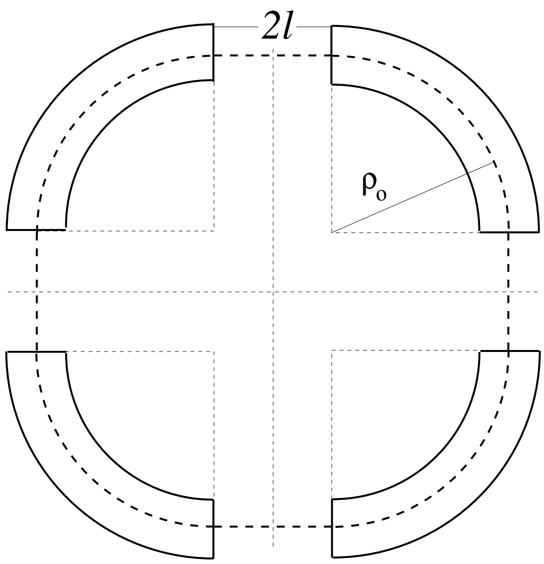

Fig. 9.23 A schematic layout of Saturne I, a $2\pi/4$ axial symmetry structure, comprised of 4 radial field index 90 deg dipoles and 4 drift spaces. The cell in the simulation exercises is taken as a $\pi/4$ quadrant: l-drift/90^o-dipole/l-drift

(c) Additional verifications regarding the model.

Table 9.2 Parameters of Saturne 1 weak focusing synchrotron [14]. ρ_0 denotes the reference bending radius in the dipole; the reference orbit, field index, wave numbers, etc., are taken along that radius

Orbit length, C	cm	6890
Equivalent radius, R	cm	1096.58
Straight section length. $2l$	cm	400
Magnetic radius, ρ_0	cm	841.93
R/ρ_0		1.30246
Field index n, nominal value		0.6
Wave numbers, ν_x; ν_y		0.724; 0.889
Stability limit		0.5 < n < 0.757
Injection energy	MeV	3.6
Field at injection	kG	0.0326
Top energy	GeV	2.94
Field at top energy	kG	14.9
Field ramp at injection	kG/s	20
Synchronous energy gain	keV/turn	1.160
RF harmonic		2

Produce a graph of the field B(s)

- along the on-momentum closed orbit, and along off-momentum chromatic closed orbits, across a cell;
- along orbits at large horizontal excursion;
- along orbits at large vertical excursion.

For all these cases, verify qualitatively, from the graphs, that $B(s)$ appears as expected.

(d) Justify considering the betatron oscillation as sinusoidal, namely,

$$y(\theta) = A\ \cos(\nu_y \theta + \phi)$$

wherein $\theta = s/R$, $R = \oint ds/2\pi$.

Find the value of the horizontal and vertical betatron functions, resulting from that approximation. Compare with the betatron functions obtained in (b).

(e) Produce an acceleration cycle from 3.6 MeV to 3 GeV, for a few particles launched on the a common $10^{-4}\,\pi$m vertical initial invariant, with small horizontal invariant. Ignore synchrotron motion (CAVITE[IOPT=3] can be used in that case). Take a peak voltage $\hat{V} = 200$ kV (unrealistic though, as it would result in a nonphysical $\dot{B}$ (Eq. 9.37)) and synchronous phase $\phi_s = 150$ deg (justify $\phi_s > \pi/2$). Add spin, using SPNTRK, in view of the next question, (f).

Check the accuracy of the betatron damping over the acceleration range, compared to theory.

How close to symplectic the numerical integration is (it is by definition *not* symplectic, being a truncated Taylor series method [25, Eq. 1.2.4]), depends on the integration step size, and on the size of the flying mesh in the DIPOLE method [25, Fig. 20]; check a possible departure of the betatron damping from theory as a function of these parameters.

Produce a graph of the the evolution of the horizontal and vertical wave numbers during the acceleration cycle.

(f) Using the raytracing material developed in (e), but for a peak voltage $\hat{V}$ = 20 kV, produce a graph of the value of the vertical spin component of the particles as a function of $G\gamma$, over the acceleration range from 3.6 MeV to 3 GeV.

Produce a graph of the average value of S_Z over that 200 particle set, as a function of $G\gamma$. Indicate on that graph the location of the resonant $G\gamma_R$ values.

(g) Based on the simulation file used in (f), simulate the acceleration of a single particle, through the intrinsic resonance $G\gamma_R = 4 - \nu_Z$, from a few thousand turns upstream to a few thousand turns downstream.

Perform this resonance crossing for five different values of the particle invariant, namely: $\varepsilon_Z/\pi = 2,\ 10,\ 20,\ 40,\ 200\,\mu$m.

Compute P_f/P_i in each case, check the dependence on ε_Z against theory. Compute the resonance strength in each case, check the dependence on ϵ_Z against theory.

Re-do this crossing simulation for a different crossing speed (take for instance $\hat{V}$ = 10 kV) and a couple of vertical invariant values, compute P_f/P_i so obtained. Check the crossing speed dependence of P_f/P_i against theory.

(h) Plot the turn-by-turn vertical spin component motion $S_Z(turn)$ across the resonance $G\gamma_R = 4 - \nu_Z$, in a weakly depolarizing case, $P_f \approx P_i$. Show that it satisfies Eq. 9.51. Match the data to the latter to get the vertical betatron tune ν_y, and the location of the resonance $G\gamma_\mathrm{R}$.

(i) Track a few particles at fixed energy, at distances from the resonance $G\gamma_R = 4 - \nu_y$ of up to a $7 \times \epsilon_R$ (this distance corresponds to 1% depolarization).

Produce on a common graph the spin motion $S_Z(turn)$ for all these particles, as observed at some azimuth along the ring.

Produce a graph of $\left\langle S_y \right\rangle|_\mathrm{turn}(\Delta)$ (as in Fig. 9.21).

Produce the vertical betatron tune ν_y, and the location of the resonance $G\gamma_\mathrm{R}$, obtained from a match of these tracking trials to the theoretical (Eq. 9.49)

$$\left\langle S_y \right\rangle(\Delta) = \frac{\Delta}{\sqrt{|\epsilon_R|^2 + \Delta^2}}$$

9.2 Construct the ZGS synchrotron. Spin Resonances

Solution: page 375

In this exercise, ZGS synchrotron is modeled in `zgoubi`, and spin resonances in this weak focusing zero-gradient synchrotron are studied.

(a) Construct an approximate model of the ZGS synchrotron, using DIPOLE. Use Figs. 9.24, 9.25 as a guidance, and parameters given in Tab. 9.3. Assume that the reference orbit is the same at all energies, on nominal radius, 2076 cm. It is judicious (although in no way an obligation) to take RM=2076 in DIPOLE. (Note that in reality, unlike the present assumption for this exercise, the reference orbit in ZGS would be moved outward during acceleration [26].)

Check the correctness of the model by producing the lattice parameters of the ring. TWISS can be used for that. Compare with the lattice parameters given in Tab. 9.3.

(b) Produce a graph of the betatron functions along the ZGS cell. Provide checks of the correctness of the computation.

Check the theoretical periodic dispersion (Eq. 9.14) against the radial distance between on- and off-momentum closed orbits obtained from tracking. Provide a plot of the dispersion function.

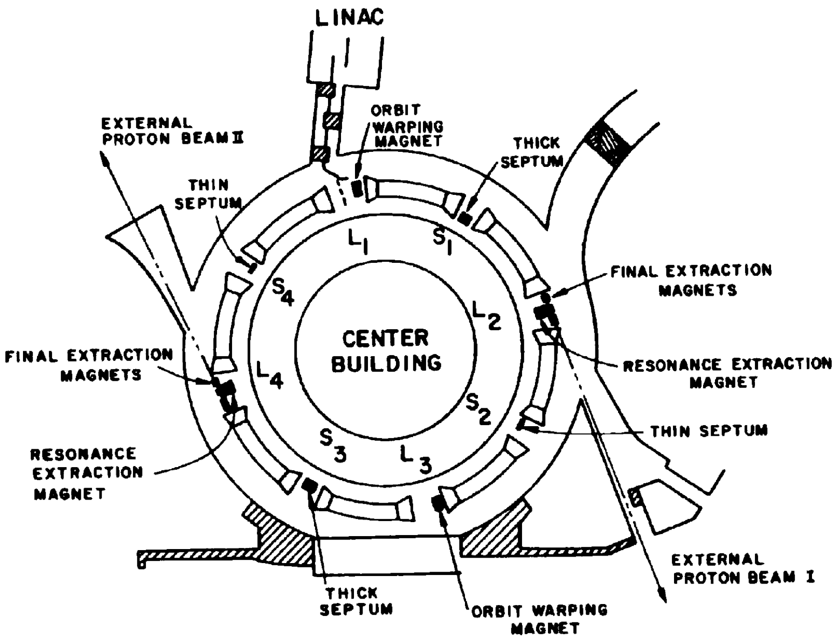

Fig. 9.24 A schematic layout of the ZGS [23], a $\pi/2$-periodic structure, comprised of 8 zero-index dipoles, 4 long and 4 short straight sections

(c) Additional verifications regarding the model.

Produce a graph of the field B(s)

- along the on-momentum closed orbit, and along off-momentum chromatic closed orbits, across a cell;

- along orbits at large horizontal excursion;

- along orbits at large vertical excursion.

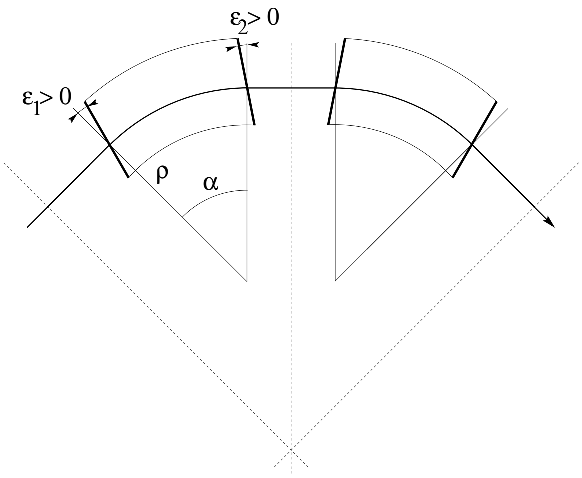

Fig. 9.25 A sketch of Saturne I cell layout. In defining the entrance and exit faces (EFBs) of the magnet, beam goes from left to right. Wedge angles at the long straight sections (ϵ_1) and at the short straight sections (ϵ_2) are different

For all these cases, verify qualitatively, from the graphs, that $B(s)$ appears as expected.

(d) Justify considering the betatron oscillation as sinusoidal, namely,

$$y(\theta) = A\ \cos(\nu_y\theta + \phi)$$

wherein $\theta = s/R$, $R = \oint ds/2\pi$.

Find the value of the horizontal and vertical betatron functions, resulting from that approximation. Compare with the betatron functions obtained in (b).

(e) Produce an acceleration cycle from 50 MeV to 17 GeV about, for a few particles launched on the a common $10^{-5}\,\pi$m vertical initial invariant, with small horizontal invariant. Ignore synchrotron motion (CAVITE[IOPT=3] can be used in that case). Take a peak voltage $\hat{V} = 200\,$kV (this is unrealistic but yields 10 times faster computing than the actual $\hat{V} = 20\,$kV, Tab. 9.3) and synchronous phase $\phi_s = 150\,$deg (justify $\phi_s > \pi/2$). Add spin, using SPNTRK, in view of the next question, (f).

Check the accuracy of the betatron damping over the acceleration range, compared to theory. How close to symplectic the numerical integration is (it is by definition *not* symplectic), depends on the integration step size, and on the size of the flying mesh in the DIPOLE method [25, Fig. 20]; check a possible departure of the betatron damping from theory as a function of these parameters.

Produce a graph of the the evolution of the horizontal and vertical wave numbers during the acceleration cycle.

Table 9.3 Parameters of the ZGS weak focusing synchrotron after Refs. [26, 27] [23, pp. 288-294,p. 716] (2nd column, when they are known) and in the present simplified model and numerical simulations (3rd column). Note that the actual orbit is skewed (moves) during ZGS acceleration cycle, tunes change as well - this is not the case in the present modeling

		From Refs. [26, 27]	**Simplified model**
Injection energy	MeV	50	
Top energy	GeV	12.5	
$G\gamma$ span		1.888387 - 25.67781	
Length of central orbit	m	171.8	170.90457
Length of straight sections, total	m	41.45	40.44
Lattice			
Wave numbers ν_x; ν_y		0.82; 0.79	0.849; 0.771
Max. β_x; β_y	m		32.5; 37.1
Magnet			
Length	m	16.3	16.30486 (magnetic)
Magnetic radius	m	21.716	20.76
Field min.; max.	kG	0.482; 21.5	0.4986; 21.54
Field index		0	
Yoke angular extent	deg	43.02590	45
Wedge angle	deg	≈10	13 and 8
RF			
Rev. frequency	MHz	0.55 - 1.75	0.551 - 1.751
RF harmonic h=$\omega_{\mathrm{rf}}/\omega_{\mathrm{rev}}$		8	
Peak voltage	kV	20	200
B-dot, nominal/max.	T/s	2.15/2.6	
Energy gain, nominal/max.	keV/turn	8.3/10	100
Synchronous phase, nominal	deg	150	
Beam			
ε_x; ε_y (at injection)	$\pi\mu$m	25; 150	
Momentum spread, rms		3×10^{-4}	
Polarization at injection	%	>75	100
Radial width of beam (90%), at inj.	inch	2.5	$\sqrt{\beta_x\varepsilon_x/\pi}=1.1$

(f) Using the raytracing material developed in (e): produce a graph of the vertical spin component of the particles, and the average value over that 200 particle set, as a function of $G\gamma$. Indicate on that graph the location of the resonant $G\gamma_R$ values.

(g) Based on the simulation file used in (f), simulate the acceleration of a single particle, through one particular intrinsic resonance, from a few thousand turns upstream to a few thousand turns downstream.

Perform this resonance crossing for different values of the particle invariant. Determine the dependence of final/initial vertical spin component value, on the invariant value; check against theory.

Re-do this crossing simulation for a different crossing speed. Check the crossing speed dependence of final/initial vertical spin component so obtained, against theory.

(h) Introduce a vertical orbit defect in the ZGS ring.

Find the closed orbit.

Accelerate a particle launched on that closed orbit, from 50 MeV to 17 GeV about, produce a graph of the vertical spin component.

Select one particular resonance, reproduce the two methods of (g) to check the location of the resonance at $G\gamma_R$ =integer, and to find its strength.

References

1. Veksler, V.: A new method of acceleration of relativistic particles. J. of Phys. USSR 9 153-158 (1945)
2. McMillan, E. M.: The Synchrotron. Phys. Rev. 68 143-144 (1945)
3. Goward, F. K., and Barnes, D. E.: Experimental 8 MeV synchrotron for electron acceleration. Nature 158, 413 (1946)
4. Kerst, D. W.: The Acceleration of Electrons by Magnetic Induction.. Phys. Rev., 60, 47-53 (1941)
5. Richardson, J.R., et al.: Frequency Modulated Cyclotron. Phys. Rev. 69: 669 (1946)
6. Sessler, A., Wilson, E.: Engines of Discovery. A Century of Particle Accelerators. World Scientific, 2007
7. Khoe, T.K., et al.: Acceleration of polarized protons to 8.5 GeV/c, Particle Accelerators, 1975, Vol. 6, pp. 213-236.
8. Credit: Brookhaven National Laboratory. https://www.flickr.com/photos/brookhavenlab/3235205168/in/album-72157611796003039/
9. Credit: Brookhaven National Laboratory. https://www.flickr.com/photos/brookhavenlab/3190757209/in/album-72157611796003039/
10. ********* TB completed **** Archives historiques CEA. Copyright CEA/Service de documentation - FAR_SA_N_00248
11. Froissart, M. and Stora, R.: Dépolarisation d'un faisceau de protons polarisés dans un synchrotron. Nucl. lnst. Meth. 7 (l960) 297.
12. Ratner, L.G. and Khoe, T.K.: Acceleration of Polarized Protons in the Zero Gradient Synchrotron. Procs. PAC 1973 Conference, Washington (1973). http://accelconf.web.cern.ch/p73/PDF/PAC1973_0217.PDF
13. Credit: CEA Saclay. *********** TB completed ***********
14. Bruck H., Debraine P., Levy-Mandel R., Lutz J., Podliasky I., Prevot F., Taieb J., Winter S.D., Maillet R., Caractéristiques principales du Synchrotron Ãă Protons de Saclay et résultats obtenus lors de la mise en route, rapport CEA no.93, CEN-Saclay, 1958.
15. Suddeth, D.E., et als.: Pole face winding equipment for eddy current correction at the Zero Gradient Synchrotron. Procs. PAC 1973 Conference, Washington (1973). http://accelconf.web.cern.ch/p73/PDF/PAC1973_0397.PDF

16. Rauchas, A.V. and Wright, A.J.: Betatron tune profile control in the Zero Gradient Synchrotron (ZGS) using the main magnet pole face windings. Procs. PAC1977 conference, IEEE Trans. on Nucl. Science, VoL.NS-24, No.3, June 1977
17. Floquet, G.: Sur les équations différentielles linéaires à coefficients périodiques. Annales scientifiques de l'E.N.S. 2e série, tome 12 (1883), p. 47-88. http://www.numdam.org/item?id=ASENS_1883_2_12__47_0
18. Bohm, D. and Foldy, L.: Theory of the Synchro-Cyclotron. Phy. Rev. 72, 649-661 (1947).
19. Cohen, D, : Feasibility of Accelerating Polarized Protons with the Argonne ZGS. Review of Scientific Instruments 33, 161 (1962).// https://doi.org/10.1063/1.1746524
20. Cho, Y., et als.: Effects of depolarizing resonances on a circulating beam of polarized protons during or storage in a synchrotron. IEEE Trans. Nuclear Science, Vol.NS-24, No.3, June 1977
21. Parker, E.F.: High Energy Polarized Deuterons at the Argonne National Laboratory Zero Gradient Synchrotron. IEEE Transactions on Nuclear Science, Vol. NS-26, No. 3, June 1979, pp 3200-3202
22. Lee, S.Y.: Spin Dynamics and Snakes in Synchrotrons. World Scientific, 1997
23. Khoe, T.K., et al.: The High Energy Polarized Beam at the ZGS. Procs. IXth Int. Conf on High Energy Accelerators, Dubna, pp. 288-294 (1974)
24. Leleux, G.: Traversée des résonances de dépolarisation. Rapport Interne LNS/GT-91-15, Saturne, Groupe Théorie, CEA Saclay (février 1991)
25. Méot, F.: Zgoubi Users' Guide. https://www.osti.gov/biblio/1062013-zgoubi-users-guide Sourceforge latest version: https://sourceforge.net/p/zgoubi/code/HEAD/tree/trunk/guide/Zgoubi.pdf
26. Foss, M.H., et al.: The Argonne ZGS Magnet. IEEE 1965, pp. 377-382, June 1965
27. Klaisner, L.A., et al.: IEEE 1965, pp. 133-137, June 1965